

# Mathematical modelling of glioblastomas invasion within the brain: a 3D multi-scale moving-boundary approach

Szabolcs Suveges <sup>1,a</sup>, Kismet Hossain-Ibrahim <sup>2,3</sup>, J. Douglas Steele <sup>4</sup>, Raluca Eftimie <sup>5</sup> and Dumitru Trucu <sup>1,b,\*</sup>

<sup>1</sup> Division of Mathematics, University of Dundee, Dundee DD1 4HN, UK; <sup>a</sup>ssuveges@dundee.ac.uk; <sup>b</sup>trucu@maths.dundee.ac.uk

<sup>2</sup> Division of Cellular and Molecular Medicine, School of Medicine, University of Dundee, Dundee, UK; kismet.ibrahim@nhs.scot

<sup>3</sup> Department of Neurosurgery, Ninewells Hospital and Medical School, NHS Tayside, Dundee, UK; kismet.ibrahim@nhs.scot

<sup>4</sup> Division of Imaging Science and Technology, Medical School, University of Dundee, Dundee, UK; d.steele@dundee.ac.uk

<sup>5</sup> Laboratoire Mathématiques de Besançon, UMR - CNRS 6623, Université de Bourgogne Franche-Comté, 16 Route de Gray, Besançon, France; raluca.eftimie@univ-fcomte.fr

\* Correspondence: trucu@maths.dundee.ac.uk

**Abstract:** Brain-related experiments are limited by nature, and so biological insights are often restricted or absent. This is particularly problematic in the context of brain cancers, which have very poor survival rates. To generate and test new biological hypotheses, researchers started using mathematical models that can simulate tumour evolution. However, most of these models focus on single-scale 2D cell dynamics, and cannot capture the complex multi-scale tumour invasion patterns in 3D brains. A particular role in these invasion patterns is likely played by the distribution of micro-fibres. To investigate explicitly the role of brain micro-fibres in the 3D invading tumours, in this study we extend a previously-introduced 2D multi-scale moving-boundary framework to take into account 3D multi-scale tumour dynamics. T1 weighted and DTI scans are used as initial conditions for our model, and to parametrise the diffusion tensor. Numerical results show that including an anisotropic diffusion term may lead in some cases (for specific micro-fibre distributions) to significant changes in tumour morphology, while in other cases it has no effect. This may be caused by the underlying brain structure and its microscopic fibre representation, which seems to influence cancer-invasion patterns through the underlying cell-adhesion process that overshadows the diffusion process.

**Keywords:** Cancer invasion, Cell adhesion, Multi-scale modelling, 3D computational modelling, T1 weighted image, DTI, Glioblastoma

**Citation:** Suveges, S.; Hossain-Ibrahim, K.; Steele, J.D.; Eftimie, R.; Trucu, D. Mathematical modelling of glioblastomas within the brain: a 3D multi-scale moving-boundary approach. *Mathematics* **2021**, *1*, 0. <https://doi.org/>

Received:  
Accepted:  
Published:

**Publisher's Note:** MDPI stays neutral with regard to jurisdictional claims in published maps and institutional affiliations.

**Copyright:** © 2021 by the authors. Submitted to *Mathematics* for possible open access publication under the terms and conditions of the Creative Commons Attribution (CC BY) license (<https://creativecommons.org/licenses/by/4.0/>).

## 1. Introduction

Glioblastoma multiforme is a highly invasive and aggressive type of brain tumour, typically with poor patient prognosis [1–7] (median survival rate is less than 1 year [8]). These tumours arise from abnormal glial cells located in the central nervous system, and shortly after their appearance they invade the surrounding tissues in a heterogeneous fashion. This heterogeneous invasion pattern leads to tumours whose outer edges are difficult or impossible to determine with current imaging technologies, including for instance *magnetic resonance imaging* (MRI) and *diffusion tensor imaging* (DTI), both of which measure the diffusion of water molecules and enable the study of brain structures.

Due to the limited experimental approaches that one can use to study the brain, researchers have started using mathematical models to provide certain biological insights

28 that otherwise would be difficult to obtain experimentally. Such models can help predict  
 29 how tumours grow for specific patients, aiding clinicians in decision-making, or they can  
 30 help test and provide new hypotheses about potential anti-tumour treatments. Math-  
 31 ematical modelling of tumours has seen significant advances over the last few decades,  
 32 which broadened our understanding of tumour dynamics and how cells interact with their  
 33 environment [9–33]. Although the majority of these models do not restrict themselves to  
 34 a specific tumour type and rather focus on general tumours, there are some models that  
 35 focus on the evolution of gliomas within the brain [34–42]. Recently, models also started  
 36 to incorporate the structure of the brain, by including MRI and DTI scans [35–37,43–46].  
 37 Even though these images are generated in 3D, most of these models are simulating the  
 38 tumour growth in 2D and only a few of them are 3D models [43,47,48]. Moreover, the ma-  
 39 jority of published models focus on tumour progression only on one spatio-temporal scale.  
 40 However, tumour progression is characterised by various biological processes occurring  
 41 on different scales, and thus their effects on the overall tumour dynamics cannot be ne-  
 42 glected. Hence, recent efforts have been made to establish new multi-scale frameworks for  
 43 tumour progression [26–30,35–37,49], which were able to capture some of these multi-scale  
 44 underlying biological processes usually involving the extracellular matrix (ECM).

45 In this paper, we extend the general 2D multi-scale moving-boundary modelling  
 46 framework introduced in [20,26] to capture the invasion of glioblastomas within a 3D  
 47 fibrous brain environment. To this end, we incorporate the information provided by both  
 48 the T1 weighted and DTI scans into our multi-scale framework and use the resulting model  
 49 to simulate numerically the growth of 3D gliomas within the brain. We focus on a few cases  
 50 showing tumour growth in different regions in the brain, with different distributions of  
 51 grey/white matter densities, which leads to different tumour invasion patterns.

52 The paper is organised as follows. First, we formulate our extended multi-scale moving  
 53 boundary framework in Section 2. Then, following a brief description of the numerical  
 54 methods, we present the computational simulation results in Section 3. Finally, in Section 4  
 55 we summarise and discuss these results.

## 56 2. Multi-Scale Modelling of the Tumour Dynamics

57 To model the evolution of glioblastomas within a 3-dimensional brain, we employ a  
 58 multi-scale moving boundary model that was initially introduced in [20] and later expanded  
 59 in several other works [26–30,49]. To account for the brain’s structure, we aim to use 3D T1  
 60 weighted and DTI scans that ultimately influence the migration of the cancer cells as well  
 61 as affect both micro-scale dynamics. Hence, here we aim to explore the impact of the brain  
 62 structure on the interlinked macro-scale and micro-scale tumour dynamics.

### 63 2.1. Macro-Scale Dynamics

64 Since in this work we extend the 2-dimensional (2D) modelling framework introduced  
 65 in [20,26], we begin by describing briefly some of the key features of this framework and  
 66 by giving a few useful notations. First, we denote by  $\Omega(t)$  the expanding 3-dimensional  
 67 (3D) tumour region that progresses over the time interval  $[0, T]$  within a maximal tissue  
 68 cube  $Y \subset \mathbb{R}^N$  with  $N = 3$ , *i.e.*,  $\Omega(t) \subset Y$ ,  $\forall t \in [0, T]$ ; see also Figure 1. Then at any macro-  
 69 scale spatio-temporal point  $(x, t) \in Y \times [0, T]$  we consider a cancer cell population  $c(x, t)$   
 70 embedded within a two-phase ECM, consisting of the non-fibre  $l(x, t)$  and fibre  $F(x, t)$   
 71 ECM phases [26–30]. On the one hand, the fibre ECM phase accounts for all major fibrous  
 72 proteins such as collagen and fibronectin, whose micro-scale distribution induces the spatial  
 73 orientation of the ECM fibres. Hence, the macro-scale spatio-temporal distribution of the  
 74 ECM fibres is represented by an oriented vector field  $\theta_f(x, t)$  that describes their spatial  
 75 bias, as well as by  $F(x, t) := \|\theta_f(x, t)\|$  which denote the amount of fibres at a macro-scale

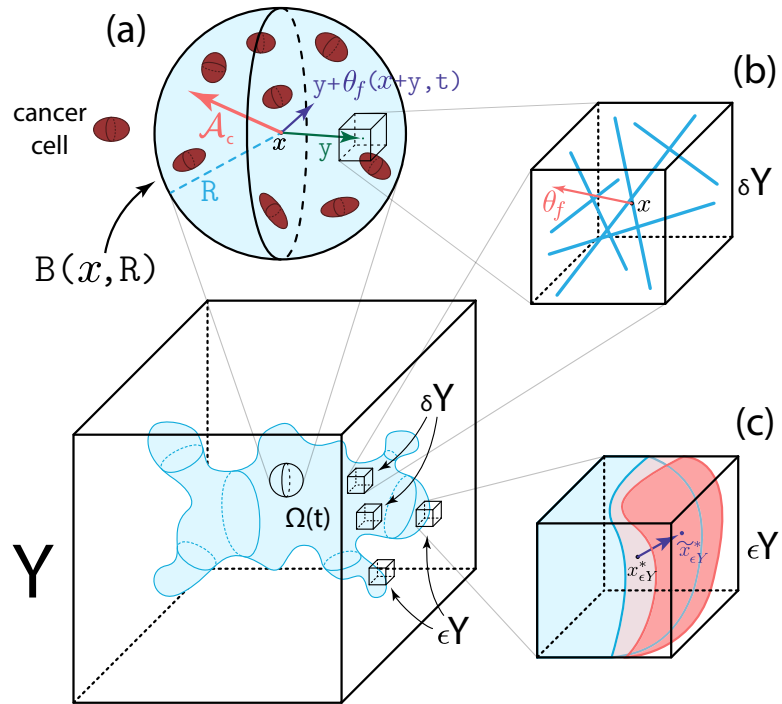


**Figure 1.** Schematics of the multi-scale model. (a) Illustration of the sensing region  $\mathbf{B}(x, R)$ , the two vectors  $y$  and  $y + \theta_f(y + x, t)$  and the overall travelling direction  $\mathcal{A}_c$ . (b) An example of a fibre micro-domain  $\delta Y(x)$  containing fibres (blue lines) that induces an overall orientation  $\theta_f(x, t)$  for  $\delta Y(x)$ . (c) An example of a boundary micro-domain  $\epsilon Y(x)$  where the blue volume represents the tumour volume at the current time-step with boundary point  $x$  and the red volume represents the evolved tumour at next time-step with shifted boundary point  $x_{\epsilon Y}^*$ .

76 point  $(x, t)$  [26–30]. On the other hand, in the non-fibre ECM phase we bundle together  
 77 every other ECM constituent such as non-fibrous proteins (for example amyloid fibrils),  
 78 enzymes, polysaccharides and extracellular  $Ca^{2+}$  ions [26–30]. Furthermore, in this new  
 79 modelling study we incorporate the structure of the brain by extracting data from DTI and  
 80 T1 weighted brain scans, and then using this data to parametrise the model. Specifically,  
 81 we denote by  $\mathbb{D}_{Water}(x)$  the water diffusion tensor that is induced by the DTI scan. Also,  
 82 we denote by  $w(x)$  the white matter density and by  $g(x)$  the grey matter density, both of  
 83 which are extracted from the T1 weighted image. Finally, for compact writing, we denote  
 84 by  $\mathbf{u}$  the global tumour vector described as

$$\mathbf{u} := (c(x, t), l(x, t), F(x, t))^T,$$

85 and by  $\rho(\mathbf{u})$  the total space occupied that is defined as

$$\rho(\mathbf{u}) := c(x, t) + l(x, t) + F(x, t).$$

### 86 2.1.1. Cancer cell population dynamics

87 To describe the spatio-temporal evolution of the cancer cell population  $c(x, t)$ , we  
 88 first assume a logistic-type growth with rate  $\mu$  [26–30, 50–52]. For the movement of this  
 89 cell population, we use the structure of the brain by taking into account both the T1  
 90 weighted and DTI scans (from the IXI Dataset [53]), as well as the various adhesion mediated

91 processes [54–59]. Hence, the spatio-temporal dynamics of the cancer cell population is  
 92 described by

$$\frac{\partial c}{\partial t} = \underbrace{\nabla \nabla : [\mathbb{D}_T(x)c]}_{\text{fully anisotropic diffusion}} - \underbrace{\nabla \cdot [c\mathcal{A}_c(x, t, \mathbf{u}, \theta_f)]}_{\text{adhesion processes}} + \underbrace{\mu c [1 - \rho(\mathbf{u})]^+}_{\text{logistic-type proliferation}}. \quad (1)$$

93 Here, the operator  $\nabla \nabla :$  denotes the full second order derivative [35], *i.e.*, it is defined as

$$\nabla \nabla : [\mathbb{D}_T(x)c] := \sum_{i,j=1}^N \frac{\partial}{\partial x_i} \frac{\partial}{\partial x_j} (\mathbb{D}_{i,j}c), \quad N = 3,$$

94 with  $\mathbb{D}_{i,j}$  denoting the components of the tumour diffusion tensor  $\mathbb{D}_T$ . Since classical  
 95 diffusion models with constant coefficient cannot capture any directional cues, as those  
 96 provided by the DTI data, in Eq. (1) we use a tensor model (involving a fully anisotropic  
 97 diffusion term) that is able to incorporate the anisotropic nature of the cancer cell movement.  
 98 These tensor models were proposed in [60–63] and have been used to mathematically model  
 99 the gliomas within the brain; see for instance [35–37]. The main idea of this approach  
 100 is to use the measured water diffusivity in the structured, fibrous brain environment  
 101 characterised by a symmetric water diffusion tensor

$$\mathbb{D}_{\text{Water}}(x) = \begin{bmatrix} d_{xx}(x) & d_{xy}(x) & d_{xz}(x) \\ d_{xy}(x) & d_{yy}(x) & d_{yz}(x) \\ d_{xz}(x) & d_{yz}(x) & d_{zz}(x) \end{bmatrix}, \quad (2)$$

102 and appropriately construct a macroscopic diffusion tensor for the cancer cell population.  
 103 Since this water tensor (2) is assumed to be symmetric, it can be diagonalised. Denoting its  
 104 eigenvalues by  $\lambda_1(x) \geq \dots \geq \lambda_N(x)$  and the associated eigenvectors by  $\phi_1(x), \dots, \phi_N(x)$ ,  
 105 we follow [37,64,65] and construct the 3D tumour diffusion tensor as

$$\mathbb{D}_T(x) := D_c D_{\text{WG}}(x) \left[ \left( r + (1-r) \left( \frac{\coth k(x)}{k(x)} - \frac{1}{k(x)^2} \right) \right) I_3 + (1-r) \left( 1 - \frac{3 \coth k(x)}{k(x)} + \frac{3}{k(x)^2} \right) \phi_1(x) \phi_1^T(x) \right]. \quad (3)$$

106 Here  $D_c > 0$  is the diffusion coefficient,  $r \in [0, 1]$  specifies the degree of isotropic diffusion,  
 107  $I_3$  denotes the  $3 \times 3$  identity matrix,  $k(x)$  is given by

$$k(x) := \mathcal{K}_{FA} FA(x),$$

108 with  $\mathcal{K}_{FA} \geq 0$  being a proportionality constant measuring the sensitivity of the cells to the  
 109 environments' direction, and  $FA(x)$  denotes the *fractional anisotropy index* [66] given by

$$FA(x) := \sqrt{\frac{(\lambda_1 - \lambda_2)^2 + (\lambda_2 - \lambda_3)^2 + (\lambda_1 - \lambda_3)^2}{2(\lambda_1^2 + \lambda_2^2 + \lambda_3^2)}}.$$

110 Finally, it is well known that the malignant glioma cells positioned in the white matter  
 111 exercise quicker motility than those situated in the grey matter [39,67–69]. To account for  
 112 this effect, in (3), we use a regulator term  $D_{\text{WG}}(\cdot)$  that is given by

$$D_{\text{WG}}(x) = a + (1-a) \left( (D_G g(x) + w(x)) * \psi_\rho \right)(x), \quad (4)$$

113 where  $0 \leq D_G \leq 1$  is the grey matter regulator coefficient,  $*$  is the convolution operator [70],  
 114  $\psi_\rho := \psi(x)/\rho^N$  denotes the standard mollifier and  $g(x)$  and  $w(x)$  are the grey and white  
 115 matter densities provided by the T1 weighted image (following an image segmentation  
 116 process). Finally,  $0 \leq a \leq 1$  is a model switching parameter distinguishes between different  
 117 cases (see Section 3).

118 In addition, the movement of the cancer cells is further biased by various adhesion  
 119 mediated process [54–59]. Due to the increasing evidence that gliomas induce a fibrous  
 120 environment within the brain [71–81], in (1) we model the overall adhesion process using  
 121 a non-local flux term that was introduced in [26] (see also [19,27–30,49,82,83] for similar  
 122 terms). Specifically, we explore the adhesive interactions of the cancer cells at  $x \in \Omega(t)$  with  
 123 other neighbouring cancer cells, with the distribution of the non-fibre ECM phase [84–87]  
 124 as well as with the oriented fibre ECM phase [88,89], all located within a sensing region  
 125  $\mathbf{B}(x, R)$  of radius  $R > 0$ . For this, we define the non-local flux term as

$$A_c(x, t, \mathbf{u}, \theta_f) := \frac{1}{R} \int_{\mathbf{B}(0, R)} \mathcal{K}(y) \left[ n(y) (\mathbf{S}_{cc} c(x+y, t) + \mathbf{S}_{cl} l(x+y, t)) \right. \\ \left. + \hat{n}(y, \theta_f(x+y, t)) \mathbf{S}_{cF} F(x+y, t) \right] [1 - \rho(\mathbf{u})]^+ dy, \quad (5)$$

126 where  $\mathbf{S}_{cc}, \mathbf{S}_{cl}, \mathbf{S}_{cF} > 0$  are the strengths of the cell-cell, cell-non-fibre ECM and cell-fibre  
 127 ECM adhesions, respectively. While we take both  $\mathbf{S}_{cl}$  and  $\mathbf{S}_{cF}$  as positive constants, we  
 128 consider the emergence of strong and stable cell-cell adhesion bonds to be positively  
 129 correlated with the level of extracellular  $Ca^{+2}$  ions (one of the non-fibre ECM component)  
 130 [90,91]. Hence, following the approach in [26–30], we describe the cell-cell adhesion strength  
 131 by

$$\mathbf{S}_{cc}(x, t) := \mathbf{S}_{min} + (\mathbf{S}_{max} - \mathbf{S}_{min}) \exp \left[ 1 - \frac{1}{1 - (1 - l(x, t))^2} \right],$$

132 where  $\mathbf{S}_{min} > 0$  and  $\mathbf{S}_{max} > 0$  are the minimum and maximum levels of  $Ca^{+2}$  ions. Further-  
 133 more, in (5) we denote by  $n(\cdot)$  and  $\hat{n}(\cdot, \cdot)$  the unit radial vector and the unit radial vector  
 134 biased by the oriented ECM fibres [26–30] defined by

$$n(y) := \begin{cases} \frac{y}{\|y\|_2} & \text{if } y \in \mathbf{B}(0, R) \setminus \{0\}, \\ 0 & \text{if } y = 0, \end{cases}$$

$$\hat{n}(y, \theta_f(x+y)) := \begin{cases} \frac{y + \theta_f(x+y, t)}{\|y + \theta_f(x+y, t)\|_2} & \text{if } y \in \mathbf{B}(0, R) \setminus \{0\}, \\ 0 & \text{if } y = 0, \end{cases}$$

135 respectively (for details on the fibre orientation  $\theta_f$  see Section 2.2.1). Also, to account for the  
 136 gradual weakening of all adhesion bonds as we move away from the centre point  $x$  within  
 137 the sensing region  $\mathbf{B}(x, t)$  in (5), we use a radially symmetric kernel  $\mathcal{K}(\cdot)$  [29,30] given by

$$\mathcal{K}(y) = \psi\left(\frac{y}{R}\right), \quad \forall y \in \mathbf{B}(0, R),$$

138 where  $\psi(\cdot)$  is the standard mollifier. Finally, in (5) a limiting term  $[1 - \rho(\mathbf{u})]^+ := \max(0, 1 -$   
 139  $\rho(\mathbf{u}))$  is used to prevent the contribution of overcrowded regions to cell migration [83]. For  
 140 a schematic of this adhesion process, we refer the reader to Figure 1(a).

141 2.1.2. Two phase ECM macro-scale dynamics

142 In addition to the cancer cell population, the rest of the macro-scale tumour dynamics  
 143 are described by the two-phase ECM. Here, both fibres and non-fibres ECM phases are  
 144 assumed to be simply described by a degradation term due to the cancer cell population.  
 145 Hence, per unit time, their dynamics is governed by

$$\begin{aligned}\frac{\partial F}{\partial t} &= -\beta_F c F, \\ \frac{\partial l}{\partial t} &= -\beta_l c l,\end{aligned}\tag{6}$$

146 where  $\beta_F > 0$  and  $\beta_l > 0$  are the degradation rates of the fibre and non-fibre ECM phases,  
 147 respectively.

148 2.1.3. The complete macro-dynamics

149 In summary, equations (1) for cancer cells dynamics and (6) for the two-phase ECM  
 150 dynamics lead to the following non-dimensional PDE system describing the evolution of  
 151 tumour at macro-scale:

$$\begin{aligned}\frac{\partial c}{\partial t} &= \nabla \nabla : [\mathbb{D}_T(x)c] - \nabla \cdot [c\mathcal{A}_c(x, t, \mathbf{u}, \theta_f)] + \mu c [1 - \rho(\mathbf{u})], \\ \frac{\partial F}{\partial t} &= -\beta_F c F, \\ \frac{\partial l}{\partial t} &= -\beta_l c l.\end{aligned}\tag{7}$$

152 To complete the macro-scale model description, we consider zero-flux boundary conditions  
 153 and appropriate initial conditions (for instance the ones given in Section 3).

154 2.2. *Micro-Scale Processes and the Double Feedback Loop*

155 Since the cancer invasion process is genuinely a multi-scale phenomenon, several  
 156 micro-scale processes are closely linked to the macro-scale dynamics [92]. In this work,  
 157 we consider two of these micro-processes, namely the rearrangement of the ECM fibres  
 158 micro-constituents [26] and the cell-scale proteolytic processes that occur at the leading  
 159 edge of the tumour [20]. Here we briefly outline these micro-processes, in addition to the  
 160 naturally arising double feedback loop that ultimately connects the micro-scale and the  
 161 macro-scale.

162 2.2.1. Two-scale representation and dynamics of fibres

163 To represent the oriented fibres on the macro-scale, we follow [26]. There, the authors  
 164 characterised not only the amount of fibres  $F(x, t)$ , but also their ability to withstand  
 165 incoming cell fluxes and forces through their spatial bias. By considering a cell-scale micro-  
 166 domain  $\delta Y(x) := x + \delta Y$  of appropriate micro-scale size  $\delta > 0$ , both of these characteristics  
 167 are induced by the microscopic fibre distribution  $f(z, t)$ , with  $z \in \delta Y(x)$ . In fact, both of  
 168 them are captured though a vector field representation  $\theta_f(x, t)$  of the ECM micro-fibres [26]  
 169 that is defined as:

$$\theta_f(x, t) := \frac{1}{\lambda(\delta Y(x))} \int_{\delta Y(x)} f(z, t) dz \cdot \frac{\theta_{f, \delta Y(x)}(x, t)}{\|\theta_{f, \delta Y(x)}(x, t)\|_2},\tag{8}$$

170 where  $\lambda(\cdot)$  is the Lebesgue measure in  $\mathbb{R}^d$  and  $\theta_{f,\delta Y(x)}(\cdot, \cdot)$  is the revolving barycentral  
 171 orientation given by [26]

$$\theta_{f,\delta Y(x)}(x, t) := \frac{\int_{\delta Y(x)} f(z, t)(z - x) dz}{\int_{\delta Y(x)} f(z, t) dz}.$$

172 Hence, the fibres' ability to withstand forces is naturally defined by this vector field repre-  
 173 sentation (8) and their amount distributed at a macro-scale point  $(x, t)$  is given by

$$F(x, t) := \|\theta_f(x, t)\|_2,$$

174 which is precisely the mean-value of the micro-fibres distributed on  $\delta Y(x)$ . Since both of  
 175 these macro-scale oriented ECM fibre characteristics ( $F(x, t)$  and  $\theta_f(x, t)$ ) that we use in  
 176 the macro-scale dynamics (7), genuinely emerge from the micro-scale distribution of the  
 177 ECM fibres  $f(z, t)$ , we refer to this link as the *fibres bottom-up* link. An illustration of a  
 178 micro-domain  $\delta Y(x)$  and its corresponding macro-scale orientation  $\theta_f(x, t)$  can be seen in  
 179 Figure 1(b).

180 On the other hand, there is also a naturally arising link that connects the macro-scale  
 181 to this micro-scale, namely the *fibres top-down* link. This connection is initiated by the  
 182 movement of the cancer cell population that trigger a rearrangement of ECM fibres micro-  
 183 constituents on each micro-domain  $\delta Y(x)$  (enabled by the secretion of matrix-degrading  
 184 enzymes that can break down various ECM proteins). Hence, using the fact that the fully  
 185 anisotropic diffusion term can be rewritten as  $\nabla \nabla : [\mathbb{D}_T(x)c] = \nabla \cdot [\mathbb{D}_T(x)\nabla c + c\nabla \cdot$   
 186  $\mathbb{D}_T(x)]$ , the fibre rearrangement process is kicked off by the cancer cell spatial flux

$$\mathcal{F}_c(x, t) := \mathbb{D}_T(x)\nabla c + c\nabla \cdot \mathbb{D}_T(x) - c\mathcal{A}_c(x, t, \mathbf{u}, \theta_f), \quad (9)$$

187 which is generated by the tumour macro-dynamics (7). Then, at any spatio-temporal point  
 188  $(x, t) \in \Omega(t) \times [0, T]$  this flux (9) gets naturally balanced in a weighted fashion by the  
 189 macro-scale ECM fibre orientation  $\theta_f(\cdot, \cdot)$ , resulting in a *rearrangement flux* [26]

$$r(\delta Y(x), t) := \omega(x, t)\mathcal{F}_c(x, t) + (1 - \omega(x, t))\theta_f(x, t), \quad (10)$$

190 with  $\omega(x, t) := c(x, t)/(c(x, t) + F(x, t))$ , that acts uniformly upon the micro-fibre distri-  
 191 bution on each micro-domain  $\delta Y(x)$ . Ultimately, this macro-scale rearrangement vector  
 192 (10) induces a micro-scale reallocation vector  $\nu_{\delta Y(x)}(z, t)$  [26], enabling us to appropriately  
 193 calculate the new position  $z^*$  of any micro-node  $z \in \delta Y(x)$  as

$$z^* := z + \nu_{\delta Y(x)}(z, t). \quad (11)$$

194 For further details on the micro-fibre rearrangement process, we refer the reader to Ap-  
 195 pendix B and [26–30].

### 196 2.2.2. MDE micro-dynamics and its links

197 The second micro-scale process that we take into consideration is the proteolytic  
 198 molecular process that occurs along the invasive edge of the tumour and is driven by the  
 199 cancer cells' ability to secrete several types of *matrix-degrading enzymes* (MDEs) (for instance,  
 200 matrix-metalloproteinases) within the proliferating rim [93–97]. Subsequent to the secretion,  
 201 these MDEs are subject to spatial transport within a cell-scale neighbourhood of the tumour



202 interface and, as a consequence, they degrade the peritumoral ECM, resulting in changes of  
 203 tumour boundary morphology [92].

204 To explore such a micro-scale process, we adopt the approach that was first introduced  
 205 in [20] where the emerging spatio-temporal MDEs micro-dynamics is considered on an  
 206 appropriate cell-scale neighbourhood of the tumour boundary  $\partial\Omega(t)$ . This neighborhood is  
 207 represented by a time-dependent bundle of overlapping cubic micro-domains  $\{\epsilon Y\}_{\epsilon Y \in \mathcal{P}(t)}$ ,  
 208 with  $\epsilon > 0$  being the size of each micro-domain  $\epsilon Y$ , which allows us to decompose the  
 209 overall MDE micro-process, transpiring on  $\bigcup_{\epsilon Y \in \mathcal{P}(t)} \epsilon Y$ , into a union of proteolytic micro-  
 210 dynamics occurring on each  $\epsilon Y$ ; see also Figure 1(c). Hence, choosing an arbitrary micro-  
 211 domain  $\epsilon Y$  and a macroscopic time instance  $t_0 \in [0, T]$ , we follow the evolution of the MDE  
 212 micro-dynamics during the time period  $[t_0, t_0 + \Delta t]$ , with appropriately chosen  $\Delta t > 0$  and  
 213 within the associated micro-domain  $\epsilon Y$ . By denoting the spatio-temporal distribution of the  
 214 MDEs by  $m(y, \tau)$  at any micro-point  $(y, \tau) \in \epsilon Y \times [0, \Delta t]$ , we observe that the cancer cell  
 215 population, located within an appropriately chosen distance  $\gamma_h > 0$  from  $y \in \epsilon Y$ , induce a  
 216 source  $h(y, \tau)$  of MDEs which can be mathematically described via a non-local term [20]

$$h(y, \tau) = \begin{cases} \frac{\int_{\mathbf{B}(y, \gamma_h) \cap \Omega(t_0)} c(x, t_0 + \tau) dy}{\lambda(\mathbf{B}(y, \gamma_h) \cap \Omega(t_0))} & y \in \epsilon Y \cap \Omega(t_0), \\ 0 & y \notin \epsilon Y \setminus (\Omega(t_0) + \{z \in Y \mid \|z\|_2 < \rho\}), \end{cases} \quad (12)$$

217 where  $0 < \rho < \gamma_h$  is a small mollification range and  $\mathbf{B}(y, \gamma_h)$  denotes the  $\|\cdot\|_\infty$  ball of  
 218 radius  $\gamma_h$  centred at a micro-node  $y$ . Since the calculation of this micro-scale MDE source  
 219 (12) directly involves the macro-scale cancer cell population  $c(\cdot, \cdot)$ , we observe a naturally  
 220 arising *MDE top-down* link that connects the macro-scale to the MDE micro-scale. In fact,  
 221 such source term (12) allows us to describe the spatio-temporal evolution of the MDEs  
 222 micro-scale distribution  $m(\cdot, \cdot)$  by [20]

$$\begin{aligned} \frac{\partial m}{\partial \tau} &= D_m \Delta m + h(y, \tau), \\ m(y, 0) &= 0, \\ \frac{\partial m}{\partial n} \Big|_{\partial \epsilon Y} &= 0, \end{aligned} \quad (13)$$

223 where  $D_m > 0$  is the constant MDEs diffusion coefficient and  $n$  denotes the outward normal  
 224 vector. As it was shown in [20], we can use the solution of the MDEs micro-dynamics (13)  
 225 to acquire both movement direction and magnitude of a tumour boundary point  $x_{\epsilon Y}^*$  within  
 226 the peritumoral area covered by the associated boundary micro-domain  $\epsilon Y$ . This ultimately  
 227 causes a boundary movement, and as a consequence we obtain a new evolved tumour  
 228 macro-domain  $\Omega(t_0 + \Delta t)$ , the link of which we refer to as the *MDE bottom-up link*. For  
 229 illustration of the boundary movement we refer the reader to Figure 1(c) and for further  
 230 details of the MDE micro dynamics see Appendix C or [20,26–30].

### 231 3. Computational Results: Numerical Simulations in 3D

232 We start this section by briefly discussing the numerical method that we use to solve  
 233 the macro-scale dynamics (7), and for details on the numerical approach used for the two  
 234 micro-scale dynamics (fibres and MDE) we refer the reader to [29,30]. Here, we use the  
 235 method of lines approach to discretise the macro-scale tumour dynamics (7) first in space,  
 236 and then, for the resulting system of ODEs, we employ a non-local predictor-corrector  
 237 scheme [26]. In this context, we carry out the spatial discretisation on a uniform grid,  
 238 where both spatial operators (fully anisotropic diffusion and adhesion) are accurately



239 approximated in a convolution-driven fashion. First, we note that the fully anisotropic  
240 diffusion term can be split into two parts

$$\nabla \nabla : [\mathbb{D}_T(x)c] = \underbrace{\nabla \cdot [\mathbb{D}_T(x)\nabla c]}_{\text{diffusive}} + \underbrace{\nabla \cdot [c\nabla \cdot \mathbb{D}_T(x)]}_{\text{advective}}, \quad (14)$$

241 which enables us to use a combination of two appropriate distinct schemes for an accurate  
242 approximation. While for the diffusive part in (14), we use the *symmetric finite difference*  
243 scheme [98,99], for the combination of the advective (14) and adhesion operators (5) (i.e.,  
244  $\nabla \cdot [c(\mathcal{A}_c(x, t, \mathbf{u}, \theta_f) + \nabla \cdot \mathbb{D}_T(x))]$ ) we use the standard *first-order upwind* finite difference  
245 scheme which ensures positivity and helps avoiding spurious oscillations in the solution.  
246 Finally, to approximate the adhesion integral  $\mathcal{A}_c(x, t, \mathbf{u}, \theta_f)$ , we consider an approach similar  
247 to [29,30], and use  $N_s$  random points located within the sensing region  $\mathbf{B}(0, R)$  and sums of  
248 discrete-convolutions.

### 249 3.1. Initial Conditions

250 For the numerical simulations presented in this paper, we consider the tissue cube  
251  $Y = [0, 4] \times [0, 4] \times [0, 4]$  with the following initial condition for the cancer cells

$$c(x, 0) = \frac{1}{2} \exp\left(\frac{-\|x\|_2^2}{0.02}\right) \cdot \chi_{\mathbf{B}((2,2,2), 0.25)},$$

252 and for the non-fibre ECM phase, the initial condition  $l(x, 0)$  is acquired by appropriately  
253 scaling the T1 weighted image via a normalising constant. Current DTI scans do not provide  
254 suitable resolution to determine the underlying micro-fibre distributions, and so here, we  
255 describe the initial micro-fibre distribution within a micro-domain  $\delta Y(x)$  as follows. When  
256 the macro-scale point  $x$  that corresponds to the micro-domain  $\delta Y(x)$  is located in the grey  
257 matter, then within  $\delta Y(x)$  we randomly draw straight lines until the ratio between the  
258 points that belong and the points that do not belong to the collection of lines is about 35% :  
259 65%. On the other hand, when the point  $x$  is located within the white matter, we use a set  
260 of predefined lines with the same point ratio (35% : 65%), ultimately achieving a random  
261 orientation within the grey matter and an aligned orientation within the white matter [100].  
262 Finally, the grey matter's fibre density is assumed to be  $1/D_G$  times smaller than the density  
263 in the white matter [100]. A schematics of this initial condition for the micro-fibres can be  
264 seen in Figure 2. Hence, we also incorporate the information about the white and grey  
265 matter tracks provided by the T1 weighted image into our micro-scale fibre distribution.

### 266 3.2. Numerical Simulations in 3D

267 Here, we present the 3D numerical solutions of the multi-scale model described above,  
268 for the parameter values listed in Table 1 in Appendix A (any alteration from these values  
269 will be stated accordingly). To display the advanced tumours at time  $50\Delta t$ , we show four  
270 panels for each simulation results. In the first three panels we show the three classical  
271 cross-section planes *i.e.*, the coronal plane (the head of the subject is viewed from behind),  
272 the axial plane (the head of the subject is viewed from above) and the sagittal plane (the  
273 head of the subject is viewed from the left). In the last panel of each simulation we show  
274 the 3D image of the brain with the embedded tumour alongside the 3D tumour in isolation.

275 The three Figures shown below investigate tumour evolution when the initial tumour  
276 starts in different regions of the brain.

277 In Figure 3 we present three distinct cases obtained by varying different parameters  
278 that appear in the tumour diffusion tensor  $\mathbb{D}_T(x)$  defined in (3). In Figure 3 (a) we assume  
279 that the tensor  $\mathbb{D}_T(x)$  depends on the white-grey matter and for that purpose we set  $r = 1$

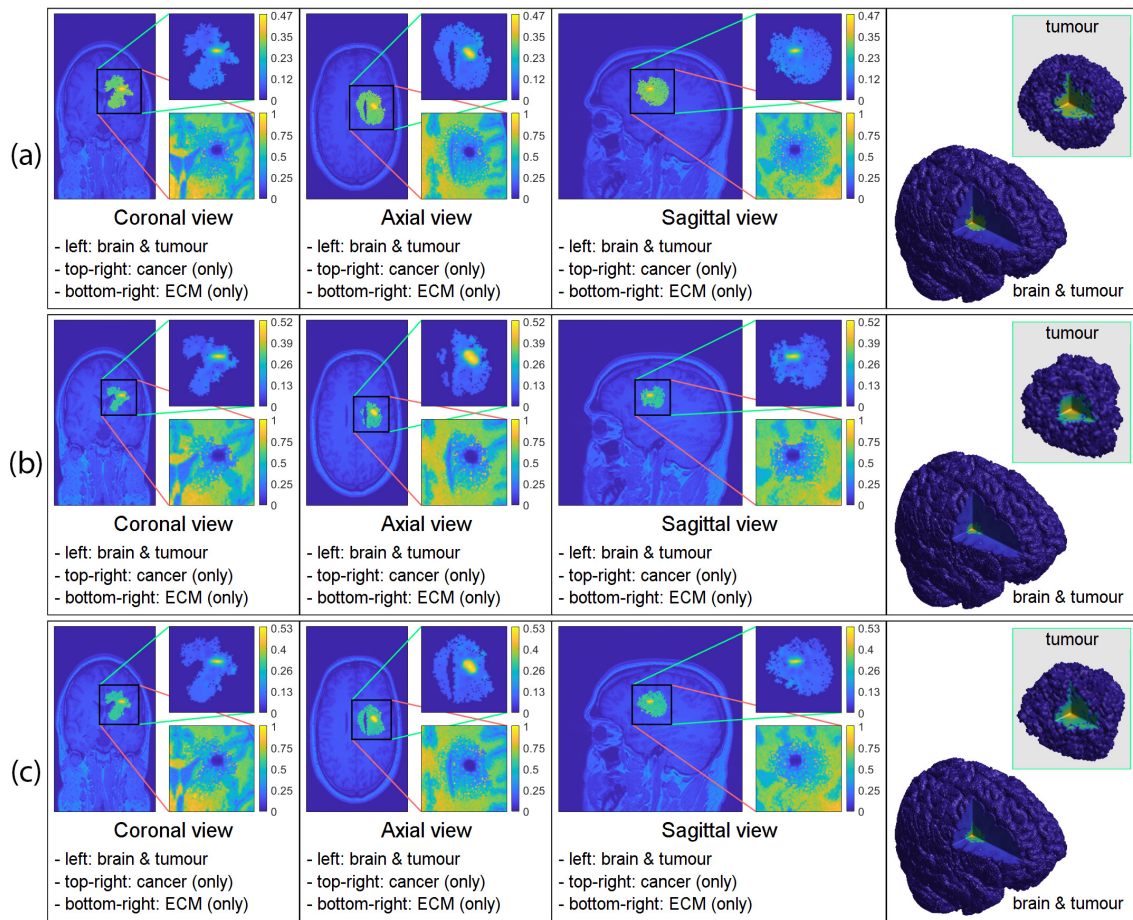


**Figure 3.** 3D computer simulation results (a) with only white-grey matter dependency ( $r = 1$ ), (b) with only DTI data used ( $D_G = 1$ ) (c) with both white-grey matter dependency and DTI data incorporated. To present the simulations, we divide each result into four panels: coronal, axial, sagittal and 3D view. Within each coronal, axial and sagittal views, we show the tumour embedded within the brain on the left, the cancer cell density on the top-right and the ECM density on the bottom-right. In the 3D view (the most right panel in each results) we show the cross-section of the whole brain with the tumour on the bottom-left corner and on the top-right corner we show the isolated tumour.

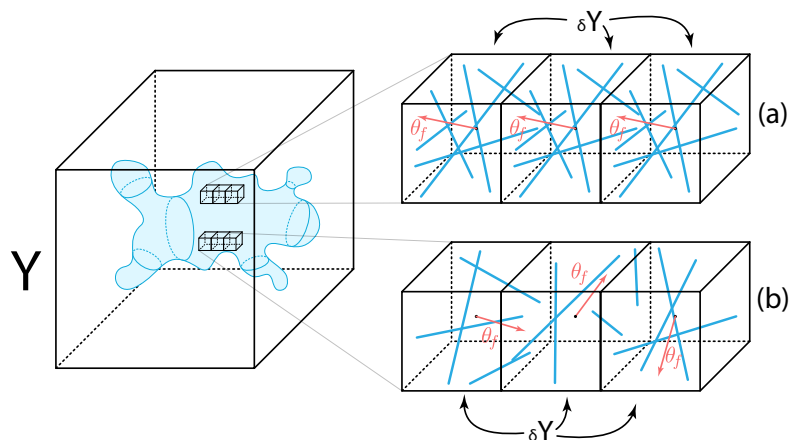


**Figure 2.** Schematics of the initial condition of the micro-fibres (blue lines) within a micro-domain  $\delta Y(x)$  of orientation  $\theta_f(x, t)$  located in the (a) white matter and in the (b) grey matter.

280 in (3) and  $a = 0$  in (4); this results in isotropic tumour diffusion. In Figure 3 (b) we use  
 281 the DTI data (i.e., there is no a-priori assumption about the preferential direction for cell  
 282 movement in white matter) and thus we set  $a = 1$  in (4) (with  $r = 0.1$ , as in Table 1); this  
 283 results in an anisotropic diffusion that does not depend explicitly on the white-grey matter.  
 In Figure 3 (c) we use both DTI data and the white-grey matter dependency ( $r = 0.1$ )

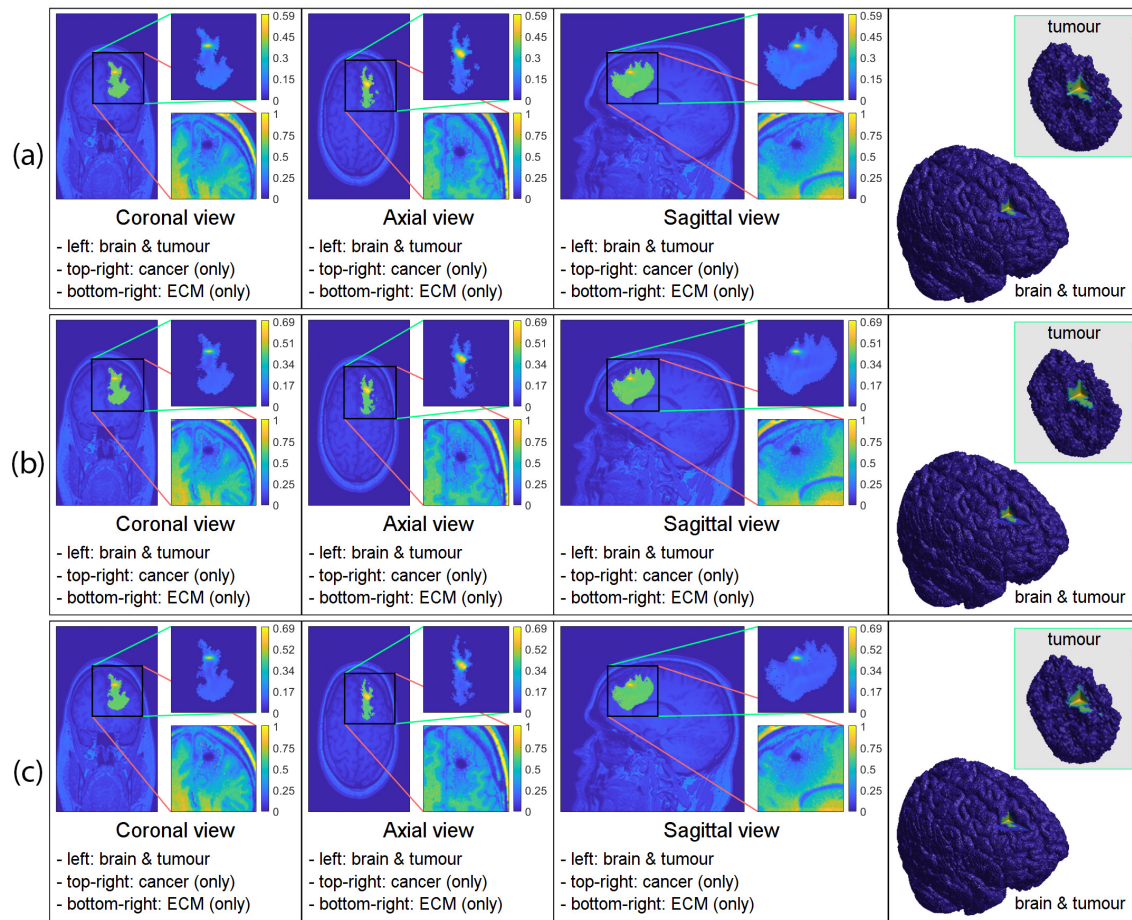


**Figure 4.** 3D computer simulation results (a) with only white-grey matter dependency ( $r = 1$ ), (b) with only DTI data used ( $D_G = 1$ ) (c) with both white-grey matter dependency and DTI data incorporated. To present the simulations, we divide each result into four panels: coronal, axial, sagittal and 3D view. Within each coronal, axial and sagittal views, we show the tumour embedded within the brain on the left, the cancer cell density on the top-right and the ECM density on the bottom-right. In the 3D view (the most right panel in each results) we show the cross-section of the whole brain with the tumour on the bottom-left corner and on the top-right corner we show the isolated tumour.

312 Similarly to Figure 3 and Figure 4, in Figure 5 we keep the same three cases (Figure 5  
 313 (a) only white-grey matter dependency, Figure 5 (b) only DTI data and Figure 5 (c) both)  
 314 while we place the initial tumour mass in the middle of the brain and present the results  
 315 at time  $50\Delta t$ . As a consequence of the initial location, we see a "butterfly" shaped tumour  
 316 that branched to both the left and right side of the brain with some asymmetry. Also, as in  
 317 Figure 4 we can see that all three cases are quite similar, and so the additional information  
 318 provided by both the DTI data and white-grey matter dependency seems to be unnecessary  
 319 for this initial condition. However, we must note that the initial conditions (fibre and  
 320 non-fibre ECM) still uses the information provided by the T1 weighted image, and so here,  
 321 we only investigate the effect of changing the diffusion tensor.

322 As we mentioned, we see significant differences between the three cases only in Figure  
 323 3. This either indicates that the anisotropic diffusion tensor provides valuable information  
 324 only in certain cases or that the initial micro-fibre density differs from the one that produced  
 325 the DTI scan (*i.e.*, the actual distribution). Since we use an artificial micro-fibre structure that  
 326 does not depend on the DTI scan which also aid the movement of the cancer cell population



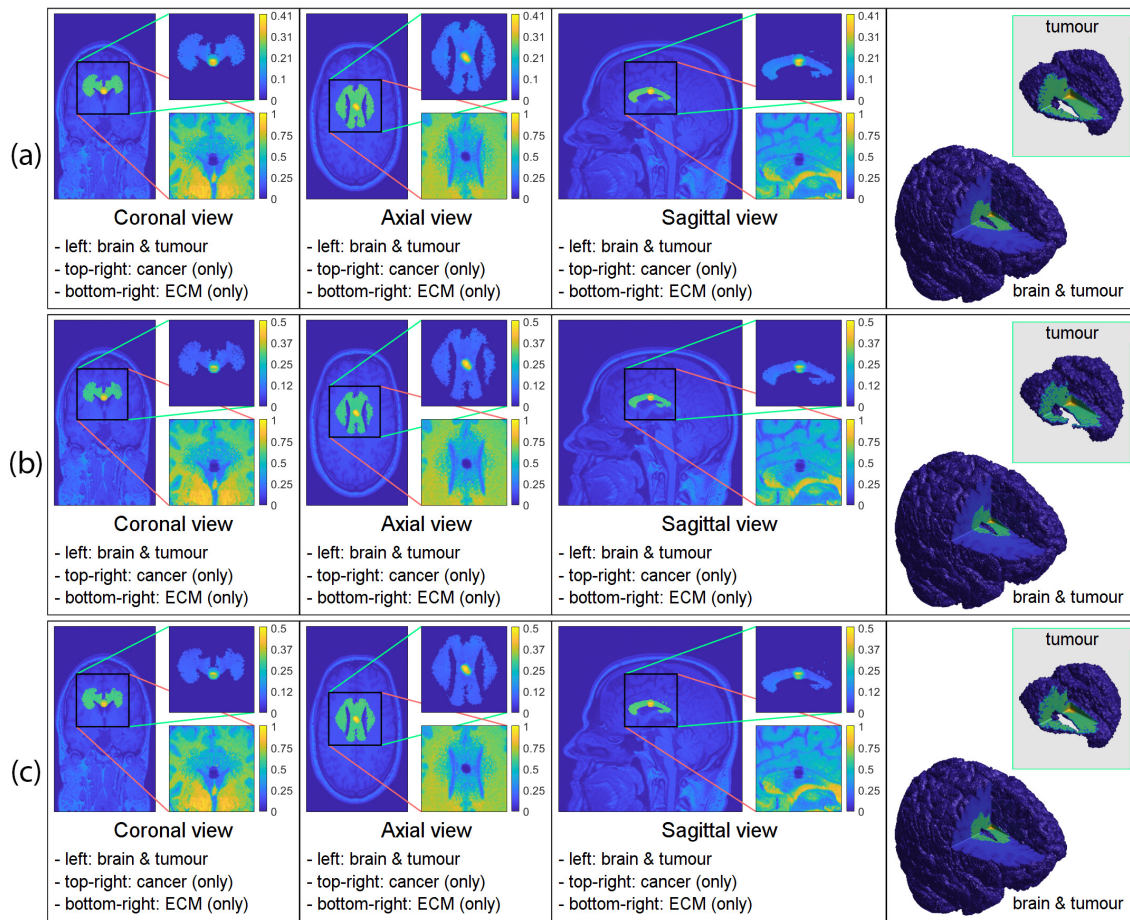


**Figure 5.** 3D computer simulation results (a) with only white-grey matter dependency ( $r = 1$ ), (b) with only DTI data used ( $D_G = 1$ ) (c) with both white-grey matter dependency and DTI data incorporated. To present the simulations, we divide each result into four panels: coronal, axial, sagittal and 3D view. Within each coronal, axial and sagittal views, we show the tumour embedded within the brain on the left, the cancer cell density on the top-right and the ECM density on the bottom-right. In the 3D view (the most right panel in each results) we show the cross-section of the whole brain with the tumour on the bottom-left corner and on the top-right corner we show the isolated tumour.

327 via the adhesion integral  $\mathcal{A}_c(\cdot, \cdot, \cdot, \cdot)$  defined in (5), it is possible that in this specific case  
 328 the micro-scale fibre distribution introduced a significantly different travelling direction  
 329 than the DTI data, resulting in discrepancies between the simulations. However, due to the  
 330 resolution of current DTI scans, it is not possible to construct a unique fibre distribution  
 331 within a micro-domain  $\delta Y(x)$ . Hence, to genuinely capture the underlying brain structures  
 332 that we can use within a mathematical model, our results suggest that DTI scans with their  
 333 present resolution may not be sufficient, and one might need to look into either obtaining  
 334 better resolution DTI scans or combine this with the strength of different technologies such  
 335 as magnetic resonance elastography. Nonetheless, this exceeds the current scope of this  
 336 work and requires further investigation.

#### 337 4. Discussion and Final Remarks

338 In this study, we have further extended the 2D multi-scale moving-boundary frame-  
 339 work previously introduced in [20,26], by developing it to 3D and applying it to the study  
 340 of glioma invasion within the brain. Since experiments are limited within the brain, we fo-

341 cused on incorporating DTI and T1 weighted scans into our framework to provide insights  
342 into the structure of the brain, the tumour, and the surrounding tissue.

343 The original framework developed in [20,26] modelled a generic tumour in a 2D  
344 setting, and so to model gliomas within a 3D brain, we extended this modelling approach  
345 by considering the structural information provided by both DTI and T1 weighted scans.  
346 We used both DTI and T1 weighted scans to construct the tumour diffusion tensor  $\mathbb{D}_T(x)$   
347 defined in (3), which resulted in a fully anisotropic diffusion term. While the T1 weighted  
348 image can give different diffusion rates based on whether the cancer cells are located in  
349 the white or grey matter, the DTI data is used to incorporate the underlying brain structure  
350 and to give higher diffusion rates along specific directions based on how the measured  
351 water molecules behaved within the brain. The T1 weighted image, which provided the  
352 white-grey matter densities, were also used in our initial conditions for both ECM phases.  
353 Hence, the initial density of the non-fibre ECM phase was taken as a normalised version  
354 of the T1 weighted image, and the initial condition of the micro-fibre distribution and  
355 magnitude were also considered to be dependent on the white-grey matter structure.  
356 Furthermore, as the available DTI scans lack the adequate resolution required to construct  
357 more appropriate micro-fibre distributions, in this work we considered a simple case where  
358 we set the fibre distributions to be either random or oriented based on whether they are  
359 positioned in the grey or white matter, respectively.

360 We used this new 3D model to explore the effects of the anisotropic diffusion term for  
361 the cancer cell population. Our numerical simulations in Figure 3 showed that including an  
362 anisotropic diffusion term may lead to significant changes in the overall tumour morphology.  
363 However, it seems that these changes depend on the position of the tumour inside the brain,  
364 as Figures 4 and 5 do not exhibit changes consistent to the ones observed between the three  
365 sub-panels of Figure 3. This may be the result of the underlying brain structure and its  
366 microscopic fibre representation, which seems to take a leading role in influencing cancer-  
367 invasion patterns through the underlying cell-adhesion process (see Eq. (5)), overshadowing  
368 this way the diffusion process. More precisely, the simplified fibre representation might not  
369 be sufficient for Figure 3, where the initial tumour was positioned in the right-middle part  
370 of the brain. However, this fibre representation might be enough for Figure 4 (with tumour  
371 positioned in the front-right of the brain) and for Figure 5 (with tumour positioned in the  
372 middle of the brain), where we did not see significant morphological differences between  
373 the three sub-panels considered in each of these figures.

374 To conclude this study, we mention that further investigation is needed to determine  
375 whether these changes in tumour invasion patterns are caused by the lack of directional  
376 information on the fibre micro-scale level or an anisotropic diffusive cell motility is necessary  
377 to better represent the invasion process. A feasible approach would also be to use a new  
378 imaging technology called magnetic resonance elastography, but this is beyond the scope  
379 of this current work. Finally, as our simulations are able to reproduce known tumour  
380 patterns of growth seen clinically, future experiments will be refined by MRI data collected  
381 prospectively from glioma patients and also incorporate the effects of their radiotherapy  
382 and chemotherapy treatments.

383 **Author Contributions:** All authors contributed to this work.

384 **Funding:** This research was funded by EPSRC DTA EP/R513192/1.

385 **Institutional Review Board Statement:** "Not applicable".

386 **Conflicts of Interest:** The authors declare no conflict of interest.

387 **Abbreviations**

388 The following abbreviations are used in this manuscript:

389

MRI	Magnetic Resonance Imaging
DTI	Diffusion Tensor Imaging
390 ECM	Extracellular matrix
MDE	Matrix degrading enzymes
PDE	Partial differential equation

### 391 Appendix A. Parameter Values

392 In Table 1, we summarise the parameter values that were used in the presented  
393 numerical simulations.

Table 1: Parameter set used for the numerical simulations.

Variable	Value	Description	Reference
$D_c$	$1.25 \times 10^{-4}$	Diffusion coeff. for the cancer cell population	[37]
$D_G$	0.25	Grey matter regulator coefficient	Estimated
$r$	0.1	Degree of randomised turning	[37]
$a$	0	Model switching parameter	Estimated
$\mathcal{K}_{FA}$	100	Cell's sensitivity to the directional information	[37]
$\mathbf{S}_{max}$	0.5	Cell-cell adhesion coeff.	[26]
$\mathbf{S}_{min}$	0.01	Minimum level of cell-cell adhesion	[29]
$\mathbf{S}_{cl}$	0.01	Cell-non-fibre adhesion coeff.	[26]
$\mathbf{S}_{cF}$	0.3	Cell-fibre adhesion coeff.	[19]
$\mu$	0.25	Proliferation coeff. for cancer cell population	[19]
$\beta_F$	1.5	Degradation coeff. of the fibre ECM	[30]
$\beta_I$	3.0	Degradation coeff. of the non-fibre ECM	[30]
$\beta$	0.8	Optimal tissue environment controller	[20]
$R$	0.15	Sensing radius	[26]
$f_{max}$	0.636	Maximum of micro-fibre density at any point	[26]
$\Delta x$	0.03125	Macro-scale spatial step-size	[20]
$\epsilon$	0.0625	Size of a boundary micro-domain $\epsilon Y(x)$	[20]
$\delta$	0.03125	Size of a fibre micro-domain $\delta Y(x)$	[26]
$N_s$	450	Number of random points used for the approximation of the adhesion integral $\mathcal{A}_c$	Estimated

### 394 Appendix B. Further Details on the Micro-Fibre Rearrangement Process

395 In Section 2.2.1, we highlighted the fact that the rearrangement of micro-fibre distri-  
396 bution  $f(z, t)$  within each  $\delta Y(x)$  is initiated by the macro-scale cell fluxes, resulting the  
397 redistribution of each micro-fibre pixel  $z$  to a new position  $z^*$ . To calculate this new position  
398  $z^*$ , we use the so-called *reallocation vector*  $v_{\delta Y(x)}(z, t)$  which takes into account the *rearrange-*  
399 *ment vector*  $r(\delta Y(x), t)$ , defined in (10), the degree of alignment between  $r(\delta Y(x), t)$  and the  
400 *barycentral position vector*  $x_{dir} := z - x$  and also incorporates the level of fibres at position  $z$ .  
401 Hence, following [26], we define it as

$$v_{\delta Y(x)}(z, t) := [x_{dir}(x) + r(\delta Y(x), t)] \cdot \frac{f(z, t)[f_{max} - f(z, t)]}{f^* + \|r(\delta Y(x), t) - x_{dir}(x)\|_2} \cdot \chi_{\{f(z, t) > 0\}},$$

402 where  $f_{max} > 0$  is the maximum level of fibres,  $f^* := f(x, t)/f_{max}$  is the saturation level and  
403  $\chi_{\{f(z, t) > 0\}}$  is the characteristic function of the micro-fibres support. To move the appropriate  
404 amount of fibres from position  $z$  to the new position  $z^*$ , given in (11), we also monitor the



405 available amount of free space at this target position  $z^*$  via a movement probability  $p_{move}$   
 406 that we define it as

$$p_{move} := \max \left( \frac{f_{max} - f(z^*, t)}{f_{max}}, 0 \right).$$

407 Consequently, we transport  $p_{move} \cdot f(z, t)$  amount of fibres to the new position  $z^*$  and the  
 408 rest  $(1 - p_{move}) \cdot f(z, t)$  remains at the original position  $z$ .

### 409 Appendix C. Further Details on the MDE micro-scale

410 Following [20], we briefly detail here the way the MDE micro-dynamics (13) deter-  
 411 mines the macro-boundary of the progressed tumour domain  $\Omega(t_0 + \Delta t)$ . To that end, on  
 412 any arbitrary boundary micro-domain  $\epsilon Y \in \mathcal{P}(t_0)$  we consider an appropriate dyadic cubes  
 413 decomposition  $\{\mathcal{D}_k\}_{\mathcal{I}}$ , and we denote the barycentre of each  $\mathcal{D}_k$  by  $y_k$ . Then, a subfamily  
 414 of small dyadic cubes  $\{\mathcal{D}_k\}_{\mathcal{J}^*}$  is sub-sampled by selecting only those dyadic cubes that  
 415 are furthest away from the boundary point  $x_{\epsilon Y}^*$  while being located outside of the tumour  
 416 domain  $\Omega(t_0)$  and carrying an above average mass of MDEs. This enables us to define  
 417 the associated direction  $\eta_{\epsilon Y}$  and displacement magnitude  $\zeta_{\epsilon Y}$  of the movement, which are  
 418 given by

$$\eta_{\epsilon Y(x_{\epsilon Y}^*)} := x_{\epsilon Y}^* + \nu \sum_{l \in \mathcal{J}^*} \left( \int_{\mathcal{D}_l} m(y, \tau) dy \right) (y_l - x_{\epsilon Y}^*), \quad \nu \in [0, \infty),$$

$$\zeta_{\epsilon Y(x_{\epsilon Y}^*)} := \sum_{l \in \mathcal{J}^*} \frac{\int_{\mathcal{D}_l} m(y, \tau) dy}{\sum_{l \in \mathcal{J}^*} \int_{\mathcal{D}_l} m(y, \tau) dy} \left| \overrightarrow{x_{\epsilon Y}^* y_l} \right|.$$

419 Although a movement direction and a displacement magnitude can be this way determined  
 420 for each boundary point  $\zeta_{\epsilon Y}$ , the actual relocation of  $\zeta_{\epsilon Y}$  only occurs if sufficient but not  
 421 complete ECM degradation will have occurred in the peritumoural region  $\epsilon Y \setminus \Omega(t_0)$ . To  
 422 quantify the amount of ECM degradation, we use a *transitional probability* that we define by

$$q(x_{\epsilon Y}^*) := \frac{\int_{\epsilon Y(x_{\epsilon Y}^*) \setminus \Omega(t_0)} m(y, \tau) dy}{\int_{\epsilon Y(x_{\epsilon Y}^*)} m(y, \tau) dy},$$

423 Then, the movement of a boundary point is exercised only when adequate but not complete  
 424 degradation of the peritumoural ECM occurs, which is characterized by the situation when  
 425 this transitional probability  $q(x_{\epsilon Y}^*)$  exceeds a certain tissue threshold  $\omega(\cdot, \cdot)$  (as defined in  
 426 [20]), namely

$$\omega(\beta, \epsilon Y) := \begin{cases} \sin \left[ \frac{\pi}{2} \left( 1 - \frac{v(x_{\epsilon Y}^*, t_0 + \Delta t)}{\beta \cdot \sup_{\zeta \in \partial \Omega(t_0)} v(\zeta, t_0 + \Delta t)} \right) \right] & \text{if } \frac{v(x_{\epsilon Y}^*, t_0 + \Delta t)}{\sup_{\zeta \in \partial \Omega(t_0)} v(\zeta, t_0 + \Delta t)} \leq \beta, \\ \sin \left[ \frac{\pi}{2(1-\beta)} \left( \frac{v(x_{\epsilon Y}^*, t_0 + \Delta t)}{\sup_{\zeta \in \partial \Omega(t_0)} v(\zeta, t_0 + \Delta t)} - \beta \right) \right] & \text{otherwise,} \end{cases}$$

427 where  $\beta \in (0, 1)$  controls the optimal level of ECM for cancer invasion and  $v(x, t) :=$   
 428  $l(x, t) + F(x, t)$ .

## References

1. Burri, S.H.; Gondi, V.; Brown, P.D.; Mehta, M.P. The Evolving Role of Tumor Treating Fields in Managing Glioblastoma. *American Journal of Clinical Oncology*, *41*, 191–196. doi:10.1097/coc.0000000000000395.
2. Davis, M. Glioblastoma: Overview of Disease and Treatment. *Clinical Journal of Oncology Nursing*, *20*, S2–S8. doi:10.1188/16.cjon.s1.2-8.
3. Klopfenstein, Q.; Truntzer, C.; Vincent, J.; Ghiringhelli, F. Cell lines and immune classification of glioblastoma define patient's prognosis. *British Journal of Cancer*, *120*, 806–814. doi:10.1038/s41416-019-0404-y.
4. Louis, D.N.; Ohgaki, H.; Wiestler, O.D.; Cavenee, W.K.; Burger, P.C.; Jouvet, A.; Scheithauer, B.W.; Kleihues, P. The 2007 WHO Classification of Tumours of the Central Nervous System. *Acta Neuropathologica*, *114*, 97–109. doi:10.1007/s00401-007-0243-4.
5. Menecur, S.; Linge, A.; Meinhardt, M.; Hering, S.; Löck, S.; Bütof, R.; Krex, D.; Schackert, G.; Temme, A.; Baumann, M.; Krause, M.; von Neubeck, C. Establishment and Characterisation of Heterotopic Patient-Derived Xenografts for Glioblastoma. *Cancers*, *12*, 871. doi:10.3390/cancers12040871.
6. Preusser, M.; de Ribaupierre, S.; Wöhrer, A.; Erridge, S.C.; Hegi, M.; Weller, M.; Stupp, R. Current concepts and management of glioblastoma. *Annals of Neurology*, *70*, 9–21. doi:10.1002/ana.22425.
7. Sottoriva, A.; Spiteri, I.; Piccirillo, S.G.M.; Touloumis, A.; Collins, V.P.; Marioni, J.C.; Curtis, C.; Watts, C.; Tavaré, S. Intratumor heterogeneity in human glioblastoma reflects cancer evolutionary dynamics. *Proceedings of the National Academy of Sciences*, *110*, 4009–4014. doi:10.1073/pnas.1219747110.
8. Brodbelt, A.; Greenberg, D.; Winters, T.; Williams, M.; Vernon, S.; Collins, V.P. Glioblastoma in England: 2007–2011. *European Journal of Cancer*, *51*, 533–542. doi:10.1016/j.ejca.2014.12.014.
9. Anderson, A.; Chaplain, M.; Newman, E.; Steele, R.; Thompson, A. Mathematical modelling of tumour invasion and metastasis. *J. Theor. Med.* **2000**, *2*, 129–154.
10. Anderson, A.R.; Hassanein, M.; Branch, K.M.; Lu, J.; Lobdell, N.A.; Maier, J.; Basanta, D.; Weidow, B.; Narasanna, A.; Arteaga, C.L.; Reynolds, A.B.; Quaranta, V.; Estrada, L.; Weaver, A.M. Microenvironmental Independence Associated with Tumor Progression. *Cancer Res* **2009**, *69*, 8797–8806. doi:10.1158/0008-5472.CAN-09-0437.
11. Anderson, A.R.A. A hybrid mathematical model of solid tumour invasion: the importance of cell adhesion. *Math. Medic. Biol.* **2005**, *22*, 163–186.
12. Basanta, D.; Simon, M.; Hatzikirou, H.; Deutsch, A. Evolutionary game theory elucidates the role of glycolysis in glioma progression and invasion. *Cell Proliferation*, *41*, 980–987. doi:10.1111/j.1365-2184.2008.00563.x.
13. Basanta, D.; Scott, J.G.; Rockne, R.; Swanson, K.R.; Anderson, A.R.A. The role of IDH1 mutated tumour cells in secondary glioblastomas: an evolutionary game theoretical view. *Physical Biology*, *8*, 015016. doi:10.1088/1478-3975/8/1/015016.
14. Böttger, K.; Hatzikirou, H.; Chauviere, A.; Deutsch, A. Investigation of the Migration/Proliferation Dichotomy and its Impact on Avascular Glioma Invasion. *Mathematical Modelling of Natural Phenomena*, *7*, 105–135. doi:10.1051/mmnp/20127106.
15. Chaplain, M.; Lolas, G. Mathematical modelling of cancer cell invasion of tissue: the role of the urokinase plasminogen activation system. *Math. Model. Meth. Appl. Sci.* **2005**, *15*, 1685–1734.
16. Chaplain, M.A.J.; Lolas, G. Mathematical modelling of cancer invasion of tissue: Dynamic heterogeneity. *Netw Heterog Media* **2006**, *1*, 399–439. doi:10.3934/nhm.2006.1.399.
17. Deakin, N.E.; Chaplain, M.A.J. Mathematical modelling of cancer cell invasion: the role of membrane-bound matrix metalloproteinases. *Front. Oncol.* **2013**, *3*, 1–9.
18. Deisboeck, T.S.; Wang, Z.; Macklin, P.; Cristini, V. Multiscale Cancer Modeling. *Annu. Rev. Biomed. Eng.* **2011**, *13*, 127–155.
19. Domschke, P.; Trucu, D.; Gerisch, A.; Chaplain, M. Mathematical modelling of cancer invasion: Implications of cell adhesion variability for tumour infiltrative growth patterns. *J. Theor. Biol.* **2014**, *361*, 41–60.
20. Trucu, D.; Lin, P.; Chaplain, M.A.J.; Wang, Y. A Multiscale Moving Boundary Model Arising In Cancer Invasion. *Multiscale Model. Simul.* **2013**, *11*, 309–335.
21. Hatzikirou, H.; Brusch, L.; Schaller, C.; Simon, M.; Deutsch, A. Prediction of traveling front behavior in a lattice-gas cellular automaton model for tumor invasion. *Computers & Mathematics with Applications*, *59*, 2326–2339. doi:10.1016/j.camwa.2009.08.041.
22. Kiran, K.L.; Jayachandran, D.; Lakshminarayanan, S. Mathematical modelling of avascular tumour growth based on diffusion of nutrients and its validation. *The Canadian Journal of Chemical Engineering* **2009**, *87*, 732–740. doi:10.1002/cjce.20204.
23. Knútsdóttir, H.; Pálsson, E.; Edelstein-Keshet, L. Mathematical model of macrophage-facilitated breast cancer cells invasion. *J. Theor. Biol.* **2014**, *357*.
24. Macklin, P.; McDougall, S.; Anderson, A.R.A.; Chaplain, M.A.J.; Cristini, V.; Lowengrub, J. Multiscale modelling and nonlinear simulation of vascular tumour growth. *J. Math. Biol.* **2009**, *58*, 765–798.
25. Mahlbacher, G.; Curtis, L.; Lowengrub, J.; Frieboes, H. Mathematical modelling of tumour-associated macrophage interactions with the cancer microenvironment. *J. Immunother. Cancer* **2018**, *6*.
26. Shuttleworth, R.; Trucu, D. Multiscale Modelling of Fibres Dynamics and Cell Adhesion within Moving Boundary Cancer Invasion. *Bulletin of Mathematical Biology* **2019**. doi:10.1007/s11538-019-00598-w.

27. Shuttleworth, R.; Trucu, D. Multiscale dynamics of a heterotypic cancer cell population within a fibrous extracellular matrix. *Journal of Theoretical Biology* **2020**, *486*, 110040. doi:10.1016/j.jtbi.2019.110040.
28. Shuttleworth, R.; Trucu, D. Cell-Scale Degradation of Peritumoural Extracellular Matrix Fibre Network and Its Role Within Tissue-Scale Cancer Invasion. *Bulletin of Mathematical Biology* **2020**, *82*, 65. doi:10.1007/s11538-020-00732-z.
29. Suveges, S.; Eftimie, R.; Trucu, D. Directionality of Macrophages Movement in Tumour Invasion: A Multiscale Moving-Boundary Approach. *Bulletin of Mathematical Biology* **2020**, *82*. doi:10.1007/s11538-020-00819-7.
30. Suveges, S.; Eftimie, R.; Trucu, D. Re-polarisation of macrophages within a multi-scale moving boundary tumour invasion model. pp. 1–50. arXiv:2103.03384.
31. Szymańska, Z.; Morales-Rodrigo, C.; Lachowicz, M.; Chaplain, M.A.J. Mathematical modelling of cancer invasion of tissue: the role and effect of nonlocal interactions. *Math Mod Meth Appl S* **2009**, *19*, 257–281.
32. Tektonidis, M.; Hatzikirou, H.; Chauvière, A.; Simon, M.; Schaller, K.; Deutsch, A. Identification of intrinsic in vitro cellular mechanisms for glioma invasion. *Journal of Theoretical Biology*, *287*, 131–147. doi:10.1016/j.jtbi.2011.07.012.
33. Xu, J.; Vilanova, G.; Gomez, H. A Mathematical Model Coupling Tumor Growth and Angiogenesis. *PLOS ONE* **2016**, *11*, e0149422. doi:10.1371/journal.pone.0149422.
34. Alfonso, J.C.L.; Köhn-Luque, A.; Stylianopoulos, T.; Feuerhake, F.; Deutsch, A.; Hatzikirou, H. Why one-size-fits-all vaso-modulatory interventions fail to control glioma invasion: in silico insights. *Scientific Reports*, *6*. doi:10.1038/srep37283.
35. Engwer, C.; Hillen, T.; Knappitsch, M.; Surulescu, C. Glioma follow white matter tracts: a multiscale DTI-based model. *Journal of Mathematical Biology*, *71*, 551–582. doi:10.1007/s00285-014-0822-7.
36. Hunt, A.; Surulescu, C. A Multiscale Modeling Approach to Glioma Invasion with Therapy. *Vietnam Journal of Mathematics*, *45*, 221–240. doi:10.1007/s10013-016-0223-x.
37. Painter, K.; Hillen, T. Mathematical modelling of glioma growth: The use of Diffusion Tensor Imaging (DTI) data to predict the anisotropic pathways of cancer invasion. *Journal of Theoretical Biology*, *323*, 25–39. doi:10.1016/j.jtbi.2013.01.014.
38. Scribner, E.; Saut, O.; Province, P.; Bag, A.; Colin, T.; Fathallah-Shaykh, H.M. Effects of Anti-Angiogenesis on Glioblastoma Growth and Migration: Model to Clinical Predictions. *PLoS ONE*, *9*, e115018. doi:10.1371/journal.pone.0115018.
39. Swanson, K.R.; Alvord, E.C.; Murray, J.D. A quantitative model for differential motility of gliomas in grey and white matter. *Cell Proliferation*, *33*, 317–329. doi:10.1046/j.1365-2184.2000.00177.x.
40. Swanson, K.R.; Rostomily, R.C.; Alvord, E.C. A mathematical modelling tool for predicting survival of individual patients following resection of glioblastoma: a proof of principle. *British Journal of Cancer*, *98*, 113–119. doi:10.1038/sj.bjc.6604125.
41. Swanson, K.R.; Rockne, R.C.; Claridge, J.; Chaplain, M.A.; Alvord, E.C.; Anderson, A.R. Quantifying the Role of Angiogenesis in Malignant Progression of Gliomas: In Silico Modeling Integrates Imaging and Histology. *Cancer Research*, *71*, 7366–7375. doi:10.1158/0008-5472.can-11-1399.
42. Syková, E.; Nicholson, C. Diffusion in Brain Extracellular Space. *Physiological Reviews*, *88*, 1277–1340. doi:10.1152/physrev.00027.2007.
43. Clatz, O.; Sermesant, M.; Bondiau, P.Y.; Delingette, H.; Warfield, S.; Malandain, G.; Ayache, N. Realistic simulation of the 3-D growth of brain tumors in MR images coupling diffusion with biomechanical deformation. *IEEE Transactions on Medical Imaging*, *24*, 1334–1346. doi:10.1109/tmi.2005.857217.
44. Cobzas, D.; Mosayebi, P.; Murtha, A.; Jagersand, M. Tumor Invasion Margin on the Riemannian Space of Brain Fibers. In *Medical Image Computing and Computer-Assisted Intervention – MICCAI 2009*; Springer Berlin Heidelberg; pp. 531–539. doi:10.1007/978-3-642-04271-3\_65.
45. Jbabdi, S.; Mandonnet, E.; Duffau, H.; Capelle, L.; Swanson, K.R.; Péligrini-Issac, M.; Guillemin, R.; Benali, H. Simulation of anisotropic growth of low-grade gliomas using diffusion tensor imaging. *Magnetic Resonance in Medicine*, *54*, 616–624. doi:10.1002/mrm.20625.
46. Konukoglu, E.; Clatz, O.; Bondiau, P.Y.; Delingette, H.; Ayache, N. Extrapolating glioma invasion margin in brain magnetic resonance images: Suggesting new irradiation margins. *Medical Image Analysis*, *14*, 111–125. doi:10.1016/j.media.2009.11.005.
47. Suarez, C.; Maglietti, F.; Colonna, M.; Breitburd, K.; Marshall, G. Mathematical Modeling of Human Glioma Growth Based on Brain Topological Structures: Study of Two Clinical Cases. *PLoS ONE*, *7*, e39616. doi:10.1371/journal.pone.0039616.
48. Yan, H.; Romero-López, M.; Benitez, L.I.; Di, K.; Frieboes, H.B.; Hughes, C.C.; Bota, D.A.; Lowengrub, J.S. 3D Mathematical Modeling of Glioblastoma Suggests That Transdifferentiated Vascular Endothelial Cells Mediate Resistance to Current Standard-of-Care Therapy. *Cancer Research*, *77*, 4171–4184. doi:10.1158/0008-5472.can-16-3094.
49. Peng, L.; Trucu, D.; Lin, P.; Thompson, A.; Chaplain, M.A.J. A multiscale mathematical model of tumour invasive growth. *Bull. Math. Biol.* **2017**, *79*, 389–429.
50. Laird, A.K. Dynamics of Tumour Growth. *British Journal of Cancer* **1964**, *13*, 490–502. doi:10.1038/bjc.1964.55.
51. Laird, A.K. Dynamics of Tumour Growth: Comparison of Growth Rates and Extrapolation of Growth Curve to One Cell. *British Journal of Cancer* **1965**, *19*, 278–291. doi:10.1038/bjc.1965.32.
52. Tjorve, K.M.C.; Tjorve, E. The use of Gompertz models in growth analyses, and new Gompertz-model approach: An addition to the Unified-Richards family. *PLOS ONE* **2017**, *12*, 1–17.
53. IXI Dataset – Information eXtraction from Images. <http://brain-development.org/ixi-dataset>.

54. Chen, Q.; Zhang, X.H.F.; Massagué, J. Macrophage Binding to Receptor VCAM-1 Transmits Survival Signals in Breast Cancer Cells that Invade the Lungs. *Cancer Cell* **2011**, *20*, 538–549. doi:10.1016/j.ccr.2011.08.025.
55. Condeelis, J.; Pollard, J.W. Macrophages: Obligate Partners for Tumor Cell Migration, Invasion, and Metastasis. *Cell* **2006**, *124*, 263–266. doi:10.1016/j.cell.2006.01.007.
56. Huda, S.; Weigel, B.; Wolf, K.; Tretiakov, K.V.; Polev, K.; Wilk, G.; Iwasa, M.; Emami, F.S.; Narojczyk, J.W.; Banaszak, M.; Soh, S.; Pilans, D.; Vahid, A.; Makurath, M.; Friedl, P.; Borisy, G.G.; Kandere-Grzybowska, K.; Grzybowski, B.A. Lévy-like movement patterns of metastatic cancer cells revealed in microfabricated systems and implicated in vivo. *Nature communications* **2018**, *9*, 4539–4539. doi:10.1038/s41467-018-06563-w.
57. Petrie, R.J.; Doyle, A.D.; Yamada, K.M. Random versus directionally persistent cell migration. *Nature Reviews Molecular Cell Biology* **2009**, *10*, 538–549. doi:10.1038/nrm2729.
58. Weiger, M.C.; Vedham, V.; Stuelten, C.H.; Shou, K.; Herrera, M.; Sato, M.; Losert, W.; Parent, C.A. Real-Time Motion Analysis Reveals Cell Directionality as an Indicator of Breast Cancer Progression. *PLOS ONE* **2013**, *8*, 1–12. doi:10.1371/journal.pone.0058859.
59. Wu, P.H.; Giri, A.; Sun, S.X.; Wirtz, D. Three-dimensional cell migration does not follow a random walk. *Proceedings of the National Academy of Sciences* **2014**, *111*, 3949–3954. doi:10.1073/pnas.1318967111.
60. Basser, P.; Mattiello, J.; LeBihan, D. Diagonal and off-diagonal components of the self-diffusion tensor: their relation to and estimation from the NMR spin-echo signal. *11th Society of Magnetic Resonance in Medicine Meeting 1222* **1992**.
61. Basser, P.; Mattiello, J.; Robert, T.; LeBihan, D. Diffusion tensor echo-planar imaging of human brain. In: *Proceedings of the SMRM 584* **1993**.
62. Basser, P.; Mattiello, J.; LeBihan, D. Estimation of the Effective Self-Diffusion Tensor from the NMR Spin Echo. *Journal of Magnetic Resonance, Series B*, *103*, 247–254. doi:10.1006/jmrb.1994.1037.
63. Basser, P.; Mattiello, J.; LeBihan, D. MR diffusion tensor spectroscopy and imaging. *Biophysical Journal*, *66*, 259–267. doi:10.1016/s0006-3495(94)80775-1.
64. Hillen, T.; ; Painter, K.J.; Swan, A.C.; Murtha, A.D.; and. Moments of von mises and fisher distributions and applications. *Mathematical Biosciences and Engineering*, *14*, 673–694. doi:10.3934/mbe.2017038.
65. Mardia, K.V. *Directional statistics*; J. Wiley.
66. Hagmann, P.; Jonasson, L.; Maeder, P.; Thiran, J.P.; Wedeen, V.J.; Meuli, R. Understanding Diffusion MR Imaging Techniques: From Scalar Diffusion-weighted Imaging to Diffusion Tensor Imaging and Beyond. *RadioGraphics*, *26*, S205–S223. doi:10.1148/rg.26si065510.
67. Chicoine, M.R.; Silbergeld, D.L. Assessment of brain tumor cell motility in vivo and in vitro. *Journal of Neurosurgery*, *82*, 615–622. doi:10.3171/jns.1995.82.4.0615.
68. Kelly, P.J.; Hunt, C. The limited value of cytoreductive surgery in elderly patients with malignant gliomas. *Neurosurgery*, *34*, 62–6; discussion 66–7.
69. Silbergeld, D.L.; Chicoine, M.R. Isolation and characterization of human malignant glioma cells from histologically normal brain. *Journal of Neurosurgery*, *86*, 525–531. doi:10.3171/jns.1997.86.3.0525.
70. Damelin, S.B.; Miller, W.J. *The Mathematics of Signal Processing*; Cambridge University Press, 2011. doi:10.1017/cbo9781139003896.
71. Gondi, C.S.; Lakka, S.S.; Yanamandra, N.; Olivero, W.C.; Dinh, D.H.; Gujrati, M.; Tung, C.H.; Weissleder, R.; Rao, J.S. Adenovirus-Mediated Expression of Antisense Urokinase Plasminogen Activator Receptor and Antisense Cathepsin B Inhibits Tumor Growth, Invasion, and Angiogenesis in Gliomas. *Cancer Research*, *64*, 4069–4077. doi:10.1158/0008-5472.can-04-1243.
72. Gregorio, I.; Braghetta, P.; Bonaldo, P.; Cescon, M. Collagen VI in healthy and diseased nervous system. *Disease Models & Mechanisms*, *11*, dmm032946. doi:10.1242/dmm.032946.
73. Kalinin, V. Cell – extracellular matrix interaction in glioma growth. In silico model. *Journal of Integrative Bioinformatics*, *17*. doi:10.1515/jib-2020-0027.
74. Mohanam, S. Biological significance of the expression of urokinase-type plasminogen activator receptors (uPARs) in brain tumors. *Frontiers in Bioscience*, *4*, d178. doi:10.2741/mohanam.
75. Persson, M.; Nedergaard, M.K.; Brandt-Larsen, M.; Skovgaard, D.; Jorgensen, J.T.; Michaelsen, S.R.; Madsen, J.; Lassen, U.; Poulsen, H.S.; Kjaer, A. Urokinase-Type Plasminogen Activator Receptor as a Potential PET Biomarker in Glioblastoma. *Journal of Nuclear Medicine*, *57*, 272–278. doi:10.2967/jnumed.115.161703.
76. Pointer, K.B.; Clark, P.A.; Schroeder, A.B.; Salamat, M.S.; Eliceiri, K.W.; Kuo, J.S. Association of collagen architecture with glioblastoma patient survival. *Journal of Neurosurgery*, *126*, 1812–1821. doi:10.3171/2016.6.jns152797.
77. Pullen, N.; Pickford, A.; Perry, M.; Jaworski, D.; Loveson, K.; Arthur, D.; Holliday, J.; Meter, T.V.; Peckham, R.; Younas, W.; Briggs, S.; MacDonald, S.; Butterfield, T.; Constantinou, M.; Fillmore, H. Current insights into matrix metalloproteinases and glioma progression: transcending the degradation boundary. *Metalloproteinases In Medicine, Volume 5*, 13–30. doi:10.2147/mnm.s105123.
78. Ramachandran, R.K.; Sørensen, M.D.; Aaberg-Jessen, C.; Hermansen, S.K.; Kristensen, B.W. Expression and prognostic impact of matrix metalloproteinase-2 (MMP-2) in astrocytomas. *PLOS ONE*, *12*, e0172234. doi:10.1371/journal.pone.0172234.
79. Veeravalli, K.K.; Rao, J.S. MMP-9 and uPAR regulated glioma cell migration. *Cell Adhesion & Migration*, *6*, 509–512. doi:10.4161/cam.21673.

80. Veeravalli, K.K.; Ponnala, S.; Chetty, C.; Tsung, A.J.; Gujrati, M.; Rao, J.S. Integrin  $\alpha 9\beta 1$ -mediated cell migration in glioblastoma via SSAT and Kir4.2 potassium channel pathway. *Cellular Signalling*, **24**, 272–281. doi:10.1016/j.cellsig.2011.09.011.
81. Young, N.; Pearl, D.K.; Brocklyn, J.R.V. Sphingosine-1-Phosphate Regulates Glioblastoma Cell Invasiveness through the Urokinase Plasminogen Activator System and CCN1/Cyr61. *Molecular Cancer Research*, **7**, 23–32. doi:10.1158/1541-7786.mcr-08-0061.
82. Armstrong, N.J.; Painter, K.J.; Sherratt, J.A. A continuum approach to modelling cell–cell adhesion. *J Theor Biol* **2006**, **243**, 98 – 113. doi:10.1016/j.jtbi.2006.05.030.
83. Gerisch, A.; Chaplain, M. Mathematical modelling of cancer cell invasion of tissue: Local and non-local models and the effect of adhesion. *J Theor Biol* **2008**, **250**, 684 – 704. doi:10.1016/j.jtbi.2007.10.026.
84. Ghosh, S.; Salot, S.; Sengupta, S.; Navalkar, A.; Ghosh, D.; Jacob, R.; Das, S.; Kumar, R.; Jha, N.N.; Sahay, S.; Mehra, S.; Mohite, G.M.; Ghosh, S.K.; Kombrabail, M.; Krishnamoorthy, G.; Chaudhari, P.; Maji, S.K. p53 amyloid formation leading to its loss of function: implications in cancer pathogenesis. *Cell Death & Differentiation* **2017**, **24**, 1784–1798. doi:10.1038/cdd.2017.105.
85. Gras, S.L. Chapter 6 - Surface- and Solution-Based Assembly of Amyloid Fibrils for Biomedical and Nanotechnology Applications. In *Engineering Aspects of Self-Organizing Materials*; Koopmans, R.J., Ed.; Academic Press, 2009; Vol. 35, *Advances in Chemical Engineering*, pp. 161 – 209. doi:10.1016/S0065-2377(08)00206-8.
86. Gras, S.L.; Tickler, A.K.; Squires, A.M.; Devlin, G.L.; Horton, M.A.; Dobson, C.M.; MacPhee, C.E. Functionalised amyloid fibrils for roles in cell adhesion. *Biomaterials* **2008**, **29**, 1553 – 1562. doi:10.1016/j.biomaterials.2007.11.028.
87. Jacob, R.S.; George, E.; Singh, P.K.; Salot, S.; Anoop, A.; Jha, N.N.; Sen, S.; Maji, S.K. Cell Adhesion on Amyloid Fibrils Lacking Integrin Recognition Motif. *Journal of Biological Chemistry* **2016**, **291**, 5278–5298. doi:10.1074/jbc.m115.678177.
88. Wolf, K.; Alexander, S.; Schacht, V.; Coussens, L.; Andrian, U.; Rheenen, J.; Deryugina, E.; Friedl, P. Collagen-based cell migration models in vitro and in vivo. *Semin Cell Dev Biol* **2009**, **20**, 931–41. doi:10.1016/j.semcdb.2009.08.005.
89. Wolf, K.; Friedl, P. Extracellular matrix determinants of proteolytic and non-proteolytic cell migration. *Tren. Cel. Biol.* **2011**, **21**, 736–744.
90. Gu, Z.; Liu, F.; Tonkova, E.A.; Lee, S.Y.; Tschumperlin, D.J.; Brenner, M.B.; Ginsberg, M.H. Soft matrix is a natural stimulator for cellular invasiveness. *Molecular Biology of the Cell* **2014**, **25**, 457–469. doi:10.1091/mbc.e13-05-0260.
91. Hofer, A.M.; Curci, S.; Doble, M.A.; Brown, E.M.; Soybel, D.I. Intercellular communication mediated by the extracellular calcium-sensing receptor. *Nat Cell Biol* **2000**, **2**, 392–398. doi:10.1038/35017020.
92. Weinberg, R.A. *The Biology of Cancer*; Garland Science: New York, 2006.
93. Hanahan, D.; Weinberg, R.A. The hallmarks of cancer. *Cell* **2000**, **100**, 57–70. doi:10.1016/S0092-8674(00)81683-9.
94. Hanahan, D.; Weinberg, R.A. Hallmarks of cancer: The next generation. *Cell* **2011**, **144**, 646–674. doi:10.1016/j.cell.2011.02.013.
95. Lu, P.; Takai, K.; Weaver, V.M.; Werb, Z. Extracellular matrix degradation and remodeling in development and disease. *Cold Spring Harb Perspect Biol.* **2011**, **3**. doi:10.1101/cshperspect.a005058.
96. Parsons, S.L.; Watson, S.A.; Brown, P.D.; Collins, H.M.; Steele, R.J. Matrix metalloproteinases. *Brit J Surg* **1997**, **84**, 160–166. doi:10.1046/j.1365-2168.1997.02719.x.
97. Pickup, M.W.; Mouw, J.K.; Weaver, V.M. The extracellular matrix modulates the hallmarks of cancer. *EMBO reports* **2014**, **15**, 1243–1253. doi:10.15252/embr.201439246.
98. van Es, B.; Koren, B.; de Blank, H.J. Finite-difference schemes for anisotropic diffusion. *Journal of Computational Physics*, **272**, 526–549. doi:10.1016/j.jcp.2014.04.046.
99. Günter, S.; Yu, Q.; Krüger, J.; Lackner, K. Modelling of heat transport in magnetised plasmas using non-aligned coordinates. *Journal of Computational Physics*, **209**, 354–370. doi:10.1016/j.jcp.2005.03.021.
100. Raffelt, D.A.; Tournier, J.D.; Smith, R.E.; Vaughan, D.N.; Jackson, G.; Ridgway, G.R.; Connelly, A. Investigating white matter fibre density and morphology using fixel-based analysis. *NeuroImage*, **144**, 58–73. doi:10.1016/j.neuroimage.2016.09.029.